

Finite Element Investigation of Quasi-Static Crack Growth in Functionally Graded Materials Using a Novel Cohesive Zone Fracture Model

Z.-H. Jin
Mem. ASME

G. H. Paulino
Mem. ASME

R. H. Dodds, Jr.
Mem. ASME

Department of Civil and Environmental
Engineering,
University of Illinois at Urbana-Champaign,
Newmark Laboratory, MC-250,
205 North Mathews Avenue
Urbana, IL 61801

This work studies mode I crack growth in ceramic/metal functionally graded materials (FGMs) using three-dimensional interface-cohesive elements based upon a new phenomenological cohesive fracture model. The local separation energies and peak tractions for the metal and ceramic constituents govern the cohesive fracture process. The model formulation introduces two cohesive gradation parameters to control the transition of fracture behavior between the constituents. Numerical values of volume fractions for the constituents specified at nodes of the finite element model set the spatial gradation of material properties with standard isoparametric interpolations inside interface elements and background solid elements to define pointwise material property values. The paper describes applications of the cohesive fracture model and computational scheme to analyze crack growth in compact tension, C(T), and single-edge notch bend, SE(B), specimens with material properties characteristic of a TiB/Ti FGM. Young's modulus and Poisson's ratio of the background solid material are determined using a self-consistent method (the background material remains linear elastic). The numerical studies demonstrate that the load to cause crack extension in the FGM compares to that for the metal and that crack growth response varies strongly with values of the cohesive gradation parameter for the metal. These results suggest the potential to calibrate the value of this parameter by matching the predicted and measured crack growth response in standard fracture mechanics specimens. [DOI: 10.1115/1.1467092]

1 Introduction

Functionally graded materials (FGMs) provide promising candidates for advanced technological applications ([1–3]). An FGM comprises a multiphase material with volume fractions of the constituent materials varying in a pre-determined profile, thus giving a nonuniform microstructure in the material with continuously graded properties. In applications involving severe thermal gradients (e.g., thermal protection structures), FGM systems exploit the heat, oxidation, and corrosion resistance typical of ceramics, and the strength and toughness typical of metals.

Cohesive fracture models have been widely used to simulate and analyze crack growth in ductile and quasi-brittle materials. In a cohesive fracture model, a narrow band termed a cohesive zone, or process zone, exists ahead of the crack front. Material behavior in the cohesive zone follows a cohesive constitutive law which relates the cohesive traction to the relative displacements of the adjacent surfaces. Crack growth occurs by progressive decohesion of the cohesive surfaces. Dugdale [4] first proposed a cohesive-type model to study ductile fracture in a thin sheet of mild steel. The Dugdale model assumes that a cracked metal sheet deforms elastically outside of the extended surfaces of the crack where a narrow band (plastic zone) of idealized zero width deforms at the constant yield stress of the material. Cohesive fracture models

have been extended to study fracture processes in quasi-brittle materials such as concrete (see, e.g., [5,6]), ductile metals (see, e.g., [7,8]), and metal matrix composites ([9]).

Though cohesive fracture models have been successfully employed to simulate failure processes in homogeneous materials and conventional composites, few studies have extended the concept to FGMs. The difficulty lies in the coexistence of different failure mechanisms in an FGM as explained in the next section. Studies of crack growth through the whole FGM component require a new phenomenological model to simulate the fracture process. Jin and Batra [10] studied crack growth in the ceramic-rich region in a ceramic/metal FGM by using both a rule of mixtures and a crack bridging model (essentially a cohesive-type model). Cai and Bao [11] investigated crack growth in a ceramic/metal graded coating by using a similar, but simpler crack bridging model. Simple applications of the rule of mixtures to an FGM significantly overestimate the fracture toughness compared to estimates from crack bridging models ([10]). Thus, it appears inappropriate to employ directly the conventional rule of mixtures to formulate the cohesive parameters of FGMs. The modifications described here provide a more realistic approach to formulate a cohesive model suitable for FGMs.

This work studies crack growth in ceramic/metal FGMs using three-dimensional interface-cohesive elements. While we are not considering the ductile deformation in the graded background material, the current study focuses on presentation of the cohesive zone model and does not incorporate the ductile separation of the graded cohesive material in the analysis of crack growth. Investigations of crack growth in ceramic/metal FGMs considering plasticity in the background material are in progress. The paper is organized as follows. Section 2 proposes a new phenomenological, cohesive fracture model developed specifically for ceramic/

Contributed by the Applied Mechanics Division of THE AMERICAN SOCIETY OF MECHANICAL ENGINEERS for publication in the ASME JOURNAL OF APPLIED MECHANICS. Manuscript received by the ASME Applied Mechanics Division, June 18, 2001; final revision, Oct. 15, 2001. Associate Editor: A. Needleman. Discussion on the paper should be addressed to the Editor, Professor Lewis T. Wheeler, Department of Mechanical Engineering, University of Houston, Houston, TX 77204-4792, and will be accepted until four months after final publication of the paper itself in the ASME JOURNAL OF APPLIED MECHANICS.

metal FGMs. In addition to the cohesive energy densities and the peak cohesive tractions of the metal and ceramic phases, two other parameters are introduced to account for the overall damage and other micromechanical effects in FGMs. Section 3 describes the three-dimensional finite element formulation with graded solid and interface-cohesive elements for applications to FGMs. Section 4 discusses the method of determining the material parameters of FGMs. Section 5 presents results of a parametric study of crack growth analyses for a titanium/titanium monoboride (Ti/TiB) FGM. Compact tension, C(T), and single-edge notched bend, SE(B), specimens are considered in the numerical simulations. Section 6 provides some conclusions and outlines ongoing work to extend the present study. The Appendix summarizes details of the tangent modulus matrix for the cohesive constitutive relation applicable to FGMs.

2 A Novel Cohesive Fracture Model

Generalization of the cohesive zone concept to model fracture in functionally graded materials (FGMs) represents a challenging task in view of the different failure mechanisms present in an FGM. In a typical ceramic/metal FGM, the ceramic-rich region may be regarded as a metal particle reinforced ceramic matrix composite, whereas the metal-rich region may be treated as a ceramic particle-reinforced metal matrix composite. Though models for the failure mechanisms of conventional composites may be adopted to study the fracture processes in the ceramic-rich or metal-rich region, the failure mechanisms operative in the interconnecting region which has no distinct matrix and inclusion phases remain unknown. This section thus proposes a volume fraction-based phenomenological cohesive fracture model suitable for engineering scale applications. The formulation first considers tensile mode (mode I) fracture of FGMs, and is then extended to general three-dimensional fracture including both tensile and shear deformations. Such volume fraction-based formulas have been used previously to calculate Young's modulus and the plastic tangent modulus of FGMs ([12,13]).

2.1 Mode I Fracture. Let σ_{fgm} denote the normal traction across the surfaces of the cohesive zone necessary to model the propagation of a macroscale crack. We propose that the cohesive traction σ of a two-phase FGM (e.g., ceramic/metal FGM) can be approximated by the following volume fraction-based formula having a simple functional form

$$\sigma_{fgm}(\mathbf{x}) = \frac{V_{met}(\mathbf{x})}{V_{met}(\mathbf{x}) + \beta_{met}[1 - V_{met}(\mathbf{x})]} \sigma_{met} + \frac{1 - V_{met}(\mathbf{x})}{1 - V_{met}(\mathbf{x}) + \beta_{cer}V_{met}(\mathbf{x})} \sigma_{cer}, \quad (1)$$

where σ_{met} is the cohesive traction of the metal, σ_{cer} the cohesive traction of the ceramic, $V_{met}(\mathbf{x})$ denotes the volume fraction of the metal, $\mathbf{x} = (x_1, x_2, x_3)$, and $\beta_{met} (\geq 1)$ and $\beta_{cer} (\geq 1)$ are two cohesive gradation parameters. The motivation to choose (1) is that the cohesive traction of the FGM will reduce to that of the metal when $V_{met} = 1$, and to that of the ceramic when $V_{met} = 0$, and the two parameters β_{met} and β_{cer} , together with the metal volume fraction (V_{met}), could describe the transition of the failure mechanism from pure ceramic to pure metal (operative in the interconnecting region which has no distinct matrix and inclusion phases).

The FGM cohesive fracture model, Eq. (1), increases the number of material-dependent parameters by two (β_{met}, β_{cer}). Values for the local separation energies and peak cohesive tractions related to the pure ductile and brittle phases are obtained using standard procedures for homogeneous materials (see [8], for example). The material-dependent parameters β_{met} and β_{cer} describe approximately the overall effect of cohesive traction reduction (from the level predicted by the rule of mixtures) and the transition between the fracture mechanisms of the metal and ceramic phases. Our preliminary computations of crack growth in a TiB/Ti

FGM indicate that β_{met} plays a far more significant role than β_{cer} , which can be simply set to unity. We anticipate that the parameter β_{met} may be experimentally calibrated by two different procedures. The first procedure determines β_{met} by matching the predicted and measured crack growth responses in standard fracture mechanics specimens of FGMs. Instead of using FGM specimens, the second procedure employs fracture specimens made of a monolithic composite each with a fixed volume fraction of the constituents. This opens the potential to calibrate β_{met} for each volume fraction level of metal and ceramic, which comprise the FGM specimens, i.e., β_{met} can become a function of V_{met} in the present model. The second calibration procedure may be particularly useful if a constant β_{met} fails to generate a match between the predicted and experimentally measured crack growth responses. Experimental determination of the β_{met} parameter is presently under investigation for zirconia/stainless steel FGMs.

For the metal phase, the cohesive traction may be derived from a free-energy density function, $\phi_{met}(\delta, q)$, in the form ([8,14–16])

$$\sigma_{met} = e \frac{\partial \phi_{met}}{\partial \delta}, \quad (2)$$

where δ is the normal displacement jump across the cohesive surfaces and q is an internal variable describing the irreversible processes of decohesion. Because in general, the shape of the cohesive traction-separation curve ($\sigma-\delta$) is not as significant as the cohesive energy density and the maximum cohesive traction in simulating fracture in ductile metals ([17]), the free-energy potential, $\phi_{met}(\delta, q)$, may be chosen in a computationally convenient exponential form ([8,14–16])

$$\phi_{met} = e \sigma_{met}^c \delta_{met}^c \left[1 - \left(1 + \frac{\delta}{\delta_{met}^c} \right) \exp \left(- \frac{\delta}{\delta_{met}^c} \right) \right]. \quad (3)$$

Under loading conditions governed by q , the cohesive traction of the metal with the above energy potential is given by

$$\sigma_{met} = e \sigma_{met}^c \left(\frac{\delta}{\delta_{met}^c} \right) \exp \left(- \frac{\delta}{\delta_{met}^c} \right), \quad (4)$$

where $e = \exp(1)$, σ_{met}^c the maximum cohesive traction, and δ_{met}^c the value of δ at $\sigma_{met} = \sigma_{met}^c$. Figure 1(a) shows a typical curve for $\sigma_{met}/\sigma_{met}^c$ versus δ/δ_{met}^c .

For quasi-brittle materials such as concrete and ceramics, the shape of the cohesive traction-separation curve may play a significant role in determining the peak load ([18]). In the present study of ceramic/metal FGMs, however, the failure mechanism of metal phase plays a dominant role. Thus, for simplicity, this study adopts the same exponential form as Eq. (4) to describe the cohesive response of the ceramic material

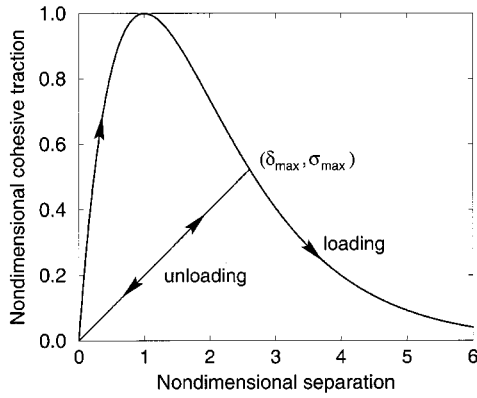
$$\sigma_{cer} = e \sigma_{cer}^c \left(\frac{\delta}{\delta_{cer}^c} \right) \exp \left(- \frac{\delta}{\delta_{cer}^c} \right), \quad (5)$$

where σ_{cer}^c is the maximum cohesive traction of the ceramic occurring at $\delta = \delta_{cer}^c$. The free-energy potential corresponding to Eq. (5) is

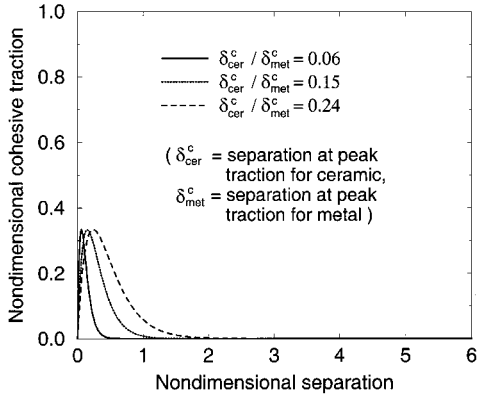
$$\phi_{cer} = e \sigma_{cer}^c \delta_{cer}^c \left[1 - \left(1 + \frac{\delta}{\delta_{cer}^c} \right) \exp \left(- \frac{\delta}{\delta_{cer}^c} \right) \right]. \quad (6)$$

Figure 1(b) shows typical curves $\sigma_{cer}/\sigma_{cer}^c$ versus δ/δ_{cer}^c for various values of $\delta_{cer}^c/\delta_{met}^c$.

By substituting Eqs. (4) and (5) into Eq. (1), we obtain the cohesive traction of the FGM under loading conditions as



(a)



(b)

Fig. 1 Normalized cohesive traction versus nondimensional separation displacement; (a) for metal, $\sigma_{met}/\sigma_{met}^c$ versus δ/δ_{met}^c ; (b) for ceramic, $\sigma_{cer}/\sigma_{met}^c$ versus δ/δ_{met}^c (where metal/ceramic strength ratio, $\sigma_{met}^c/\sigma_{cer}^c$, is taken to be 3)

$$\sigma_{fgm}(\mathbf{x}) = \frac{V_{met}(\mathbf{x})}{V_{met}(\mathbf{x}) + \beta_{met}[1 - V_{met}(\mathbf{x})]} e \sigma_{met}^c \left(\frac{\delta}{\delta_{met}^c} \right) \exp\left(-\frac{\delta}{\delta_{met}^c}\right) + \frac{1 - V_{met}(\mathbf{x})}{1 - V_{met}(\mathbf{x}) + \beta_{cer} V_{met}(\mathbf{x})} e \sigma_{cer}^c \left(\frac{\delta}{\delta_{cer}^c} \right) \exp\left(-\frac{\delta}{\delta_{cer}^c}\right). \quad (7)$$

The free-energy density function corresponding to the above cohesive traction is

$$\begin{aligned} \phi_{fgm}(\mathbf{x}, \delta, q) = & \frac{V_{met}(\mathbf{x})}{V_{met}(\mathbf{x}) + \beta_{met}[1 - V_{met}(\mathbf{x})]} \\ & \times e \sigma_{met}^c \delta_{met}^c \left[1 - \left(1 + \frac{\delta}{\delta_{met}^c} \right) \exp\left(-\frac{\delta}{\delta_{met}^c}\right) \right] \\ & + \frac{1 - V_{met}(\mathbf{x})}{1 - V_{met}(\mathbf{x}) + \beta_{cer} V_{met}(\mathbf{x})} \\ & \times e \sigma_{cer}^c \delta_{cer}^c \left[1 - \left(1 + \frac{\delta}{\delta_{cer}^c} \right) \exp\left(-\frac{\delta}{\delta_{cer}^c}\right) \right]. \quad (8) \end{aligned}$$

As often assumed for homogeneous materials, the cohesive law of the FGM also follows an irreversible path. The internal variable describing the irreversible processes, q , is chosen as δ_{max} , the maximum opening displacement attained. For updating of the cohesive stresses, the loading condition is defined by

$$\delta = \delta_{max} \quad \text{and} \quad \dot{\delta} \geq 0, \quad (9)$$

where $\dot{\delta}$ denotes the rate of δ . The unloading condition is then described by

$$\delta < \delta_{max} \quad \text{or} \quad \dot{\delta} < 0. \quad (10)$$

Following the cohesive law for homogeneous materials, the unloading curve follows the linear relation

$$\sigma_{fgm} = \left(\frac{\sigma_{max}}{\delta_{max}} \right) \delta, \quad \text{if} \quad \delta < \delta_{max} \quad \text{or} \quad \dot{\delta} < 0, \quad (11)$$

where σ_{max} is the value of σ_{fgm} at $\delta = \delta_{max}$ calculated from Eq. (7). We note that the irreversibility of the above cohesive law does not influence the results reported in Section 5 since we have only studied crack growth under monotonic loading conditions.

2.2 Three-Dimensional Mixed Mode Fracture. For general three-dimensional mixed mode fracture problems, an effective opening displacement jump is introduced ([19])

$$\delta_{eff} = \sqrt{\delta_n^2 + \eta^2 \delta_s^2}, \quad (12)$$

where δ_n and δ_s are the normal and tangential displacement jumps across the cohesive surfaces. The parameter η assigns different weights to the opening and sliding displacements (η is usually taken as $\sqrt{2}$). Similarly, an effective cohesive traction may be introduced ([19])

$$\sigma_{eff} = \sqrt{\sigma_n^2 + \eta^{-2} \sigma_s^2}, \quad (13)$$

where σ_n and σ_s are the normal and shear tractions across the cohesive surfaces. Here we assume that resistance of the cohesive surfaces to relative sliding is isotropic in the cohesive (tangent) plane so that

$$\delta_s = \sqrt{\delta_{s1}^2 + \delta_{s2}^2}, \quad (14)$$

$$\sigma_s = \sqrt{\sigma_{s1}^2 + \sigma_{s2}^2}, \quad (15)$$

where δ_{s1} and δ_{s2} are the two relative sliding displacements across the cohesive surfaces, and σ_{s1} and σ_{s2} are the two shear tractions.

With the introduction of the above effective traction and displacement, a free-energy potential in three dimensions is assumed to exist in the same form as that for the mode I case (8), i.e.,

$$\begin{aligned} \phi_{fgm}(\mathbf{x}, \delta_{eff}, \delta_{eff}^{max}) = & \frac{V_{met}(\mathbf{x})}{V_{met}(\mathbf{x}) + \beta_{met}[1 - V_{met}(\mathbf{x})]} \\ & \times e \sigma_{met}^c \delta_{met}^c \left[1 - \left(1 + \frac{\delta_{eff}}{\delta_{met}^c} \right) \exp\left(-\frac{\delta_{eff}}{\delta_{met}^c}\right) \right] \\ & + \frac{1 - V_{met}(\mathbf{x})}{1 - V_{met}(\mathbf{x}) + \beta_{cer} V_{met}(\mathbf{x})} \\ & \times e \sigma_{cer}^c \delta_{cer}^c \left[1 - \left(1 + \frac{\delta_{eff}}{\delta_{cer}^c} \right) \exp\left(-\frac{\delta_{eff}}{\delta_{cer}^c}\right) \right], \quad (16) \end{aligned}$$

where δ_{eff}^{max} is the maximum value of δ_{eff} attained. The cohesive law for general three-dimensional deformations is then formulated as follows:

$$\sigma_n = \frac{\partial \phi_{fgm}}{\partial \delta_n} = \frac{\partial \phi_{fgm}}{\partial \delta_{eff}} \frac{\partial \delta_{eff}}{\partial \delta_n} = \left(\frac{\sigma_{eff}}{\delta_{eff}} \right) \delta_n, \quad (17)$$

$$\sigma_s = \frac{\partial \phi_{fgm}}{\partial \delta_s} = \frac{\partial \phi_{fgm}}{\partial \delta_{eff}} \frac{\partial \delta_{eff}}{\partial \delta_s} = \eta^2 \left(\frac{\sigma_{eff}}{\delta_{eff}} \right) \delta_s,$$

where

$$\sigma_{\text{eff}} = \frac{\partial \phi_{\text{fgm}}}{\partial \delta_{\text{eff}}} = \frac{V_{\text{met}}(\mathbf{x})}{V_{\text{met}}(\mathbf{x}) + \beta_{\text{met}}[1 - V_{\text{met}}(\mathbf{x})]} e \sigma_{\text{met}}^c \left(\frac{\delta}{\delta_{\text{met}}^c} \right) \times \exp\left(-\frac{\delta}{\delta_{\text{met}}^c}\right) + \frac{1 - V_{\text{met}}(\mathbf{x})}{1 - V_{\text{met}}(\mathbf{x}) + \beta_{\text{cer}} V_{\text{met}}(\mathbf{x})} \times e \sigma_{\text{cer}}^c \left(\frac{\delta}{\delta_{\text{cer}}^c} \right) \exp\left(-\frac{\delta}{\delta_{\text{cer}}^c}\right),$$

if $\delta_{\text{eff}} = \delta_{\text{eff}}^{\text{max}}$ and $\dot{\delta}_{\text{eff}} \geq 0$,

for the loading case, and

$$\sigma_{\text{eff}} = \left(\frac{\sigma_{\text{eff}}^{\text{max}}}{\delta_{\text{eff}}^{\text{max}}} \right) \delta_{\text{eff}}, \quad \text{if } \delta_{\text{eff}} < \delta_{\text{eff}}^{\text{max}} \text{ or } \dot{\delta}_{\text{eff}} < 0, \quad (19)$$

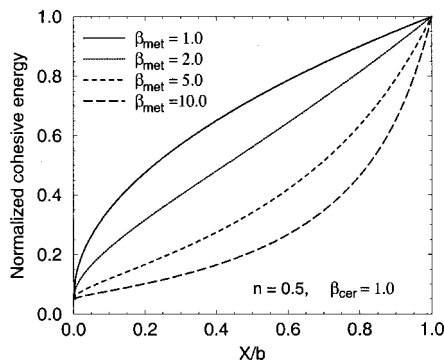
for the unloading case, where $\sigma_{\text{eff}}^{\text{max}}$ is the value of σ_{eff} at $\delta_{\text{eff}} = \delta_{\text{eff}}^{\text{max}}$ calculated from Eq. (18).

2.3 Cohesive Energy Density. The cohesive energy density, or the work of separation per unit area of cohesive surface, is defined by

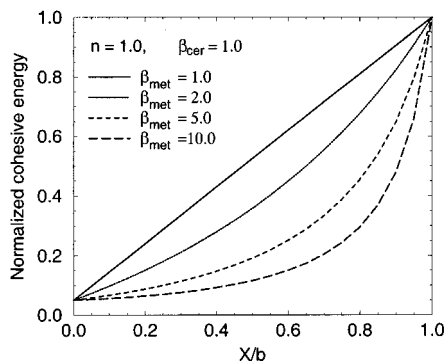
$$\Gamma_{\text{fgm}}^c = \int_0^\infty \sigma(\delta_{\text{eff}}) d\delta_{\text{eff}}. \quad (20)$$

By substituting Eq. (18) into the above equation, we obtain

$$\Gamma_{\text{fgm}}^c(\mathbf{x}) = \frac{V_{\text{met}}(\mathbf{x})}{V_{\text{met}}(\mathbf{x}) + \beta_{\text{met}}[1 - V_{\text{met}}(\mathbf{x})]} \Gamma_{\text{met}}^c + \frac{1 - V_{\text{met}}(\mathbf{x})}{1 - V_{\text{met}}(\mathbf{x}) + \beta_{\text{cer}} V_{\text{met}}(\mathbf{x})} \Gamma_{\text{cer}}^c, \quad (21)$$



(a)



(b)

Fig. 2 Normalized cohesive energy density $\Gamma_{\text{fgm}}^c / \Gamma_{\text{met}}^c$ ($\Gamma_{\text{cer}}^c / \Gamma_{\text{met}}^c = 0.05$, $V_{\text{met}}(X) = (X/b)^n$), (a) $n=0.5$; (b) $n=1.0$

where Γ_{met}^c and Γ_{cer}^c are the cohesive energy densities of the metal and ceramic phases, respectively,

$$\Gamma_{\text{met}}^c = e \sigma_{\text{met}}^c \delta_{\text{met}}^c, \quad \Gamma_{\text{cer}}^c = e \sigma_{\text{cer}}^c \delta_{\text{cer}}^c. \quad (22)$$

Equation (21) shows that the cohesive energy density follows the same rule as that of the cohesive traction. Figure 2 shows the normalized cohesive energy density $\Gamma_{\text{fgm}}^c / \Gamma_{\text{met}}^c$ versus the nondimensional coordinate X/b for a ceramic/metal FGM with metal volume fraction $V_{\text{met}} = (X/b)^n$, where X is the gradation direction and b is a geometrical parameter, e.g., the thickness of the FGM specimen. In these figures, the energy ratio, $\Gamma_{\text{cer}}^c / \Gamma_{\text{met}}^c$ is assumed 0.05 with β_{cer} taken as 1.0. The cohesive energy of the FGM decreases markedly with increasing β_{met} .

3 Three-Dimensional Finite Element Modeling of Functionally Graded Materials

This section describes the small-displacement formulation of both the three-dimensional solid element and the interface-cohesive element with graded material properties. In the present study, the solid elements remain linearly elastic but the material properties (Young's modulus and Poisson's ratio) may vary within the element and thus graded elements are employed (Kim and Paulino [20]). For the cohesive element, the material properties follow the functionally graded cohesive law described in Section 2. Figure 3 illustrates the three-dimensional interface-cohesive and solid elements used in the present work. The interface-cohesive element consists of two four-node bilinear isoparametric surfaces. Nodes 1–4 lie on one surface of the element while nodes 5–8 lie on the opposite surface. The two surfaces initially occupy the same location. When the whole body deforms, the two surfaces undergo both normal and tangential displacements relative to each other. The cohesive tractions corresponding to the relative displacements follow the constitutive relations (17)–(19), and thus maintain the two surfaces in a “cohesive” state.

Now first consider the stiffness matrix of the isoparametric solid element. Denote by $N_i(\xi, \eta, \zeta)$ ($i=1, 2, \dots, m$) the standard shape functions of the solid element ([21]), where m is the number of the nodes of the element. The element stiffness matrix is given by

$$\mathbf{K} = \int_{-1}^1 \int_{-1}^1 \int_{-1}^1 \mathbf{B}^T \mathbf{D} \mathbf{B} J_0 d\xi d\eta d\zeta, \quad (23)$$

where \mathbf{B} is the strain-displacement matrix, J_0 is the usual Jacobian of the transformation between parametric (ξ, η, ζ) and Cartesian coordinates (x_1, x_2, x_3) , and \mathbf{D} is the elastic stiffness matrix. For functionally graded materials (FGMs), the \mathbf{D} matrix depends on

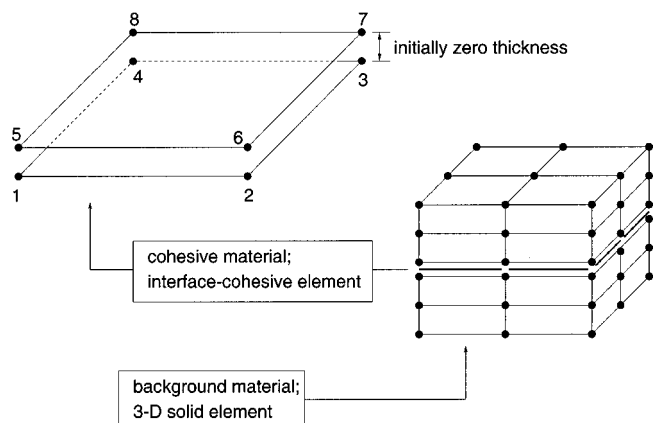


Fig. 3 Interface-cohesive and three-dimensional solid elements

spatial position. To calculate the Young's modulus and the Poisson's ratio in the solid element, we use the following interpolation:

$$E = \sum_{i=1}^m N_i E_i, \quad \nu = \sum_{i=1}^m N_i \nu_i, \quad (24)$$

where E_i and $\nu_i (i=1,2,\dots,m)$ are the values of the Young's modulus and the Poisson's ratio at nodal points, respectively.

Turning to the cohesive element, the tangent stiffness matrix is given by ([8]),

$$\mathbf{K}_T = \int_{-1}^1 \int_{-1}^1 \mathbf{B}_{\text{coh}}^T \mathbf{D}_{\text{coh}} \mathbf{B}_{\text{coh}} J_0 d\eta d\zeta, \quad (25)$$

where \mathbf{B}_{coh} extracts the relative displacement jumps within the cohesive element from the nodal displacements ([8]), J_0 is the Jacobian of the transformation between parametric (η, ζ) and Cartesian coordinates (s_1, s_2) in the tangent plane of the cohesive element, and \mathbf{D}_{coh} is the tangent modulus matrix of the cohesive law (17)–(19) which can be found in the Appendix. For FGMs, Eq. (18) and Eqs. (34) and (35) in the Appendix show that the \mathbf{D}_{coh} matrix depends on spatial position through the graded volume fraction of the metal phase, V_{met} , in a ceramic/metal FGM. In this study, V_{met} is also approximated by the standard interpolation

$$V_{\text{met}} = \sum_{i=1}^4 N_i V_{\text{met}}^i, \quad (26)$$

where $V_{\text{met}}^i (i=1,2,3,4)$ are the values of V_{met} at the nodal points of the interface-cohesive elements. The present formulation is fully isoparametric in which the same shape functions interpolate the displacements, the geometry and the material parameters. Such a generalized isoparametric formulation has been presented by Kim and Paulino [20].

4 Functionally Graded Material Properties

This section describes the techniques adopted to obtain the properties for both the background functionally graded materials (FGM) and cohesive FGM materials. One of the advantages of the present methodology is that each model is developed separately for each material, as described below. This feature introduces significant flexibility in modeling the actual material behavior.

4.1 Background Material Properties. Consider an FGM as a two-phase composite with graded volume fractions of its constituent phases. The effective properties of an FGM should be calculated from those of the constituent materials and the volume fractions by means of a micromechanical model. Though such a model is not available as yet for FGMs, some models for conventional homogeneous composite materials, for example, the self-consistent scheme, may be used for FGMs with reasonable accuracy ([22]). In this study, we use the self-consistent scheme ([23]) to calculate the effective elastic properties of the FGM. The shear and bulk moduli μ_{fgm} and K_{fgm} of the FGM are thus calculated by the following system of equations:

$$\begin{aligned} & (\mu_{\text{fgm}} - \mu_{\text{met}})(\mu_{\text{fgm}} - \mu_{\text{cer}}) \left[\frac{V_{\text{met}} K_{\text{met}}}{K_{\text{met}} + 4\mu_{\text{fgm}}/3} + \frac{(1 - V_{\text{met}}) K_{\text{cer}}}{K_{\text{cer}} + 4\mu_{\text{fgm}}/3} + 2 \right] \\ & + 5[V_{\text{met}} \mu_{\text{cer}} (\mu_{\text{fgm}} - \mu_{\text{met}}) + (1 - V_{\text{met}}) \mu_{\text{met}} (\mu_{\text{fgm}} - \mu_{\text{cer}})] \\ & = 0, \end{aligned} \quad (27)$$

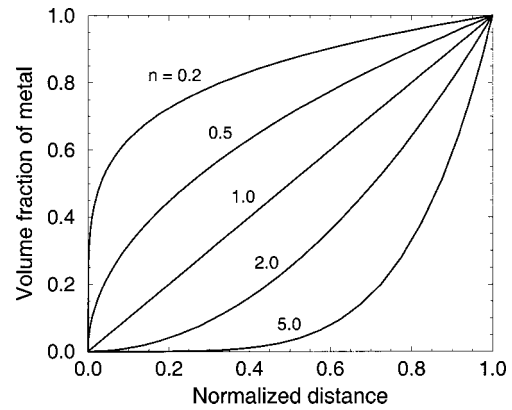


Fig. 4 Volume fraction of metallic phase in a ceramic/metal functionally graded material (FGM)

$$\begin{aligned} K_{\text{fgm}} = & -\frac{4}{3} \mu_{\text{fgm}} \\ & + \frac{(K_{\text{met}} + 4\mu_{\text{fgm}}/3)(K_{\text{cer}} + 4\mu_{\text{fgm}}/3)}{V_{\text{met}}(K_{\text{cer}} + 4\mu_{\text{fgm}}/3) + (1 - V_{\text{met}})(K_{\text{met}} + 4\mu_{\text{fgm}}/3)}. \end{aligned} \quad (28)$$

The Young's modulus E_{fgm} and the Poisson's ratio ν_{fgm} of the FGM are then determined from the following relations:

$$E_{\text{fgm}} = \frac{9\mu_{\text{fgm}} K_{\text{fgm}}}{\mu_{\text{fgm}} + 3K_{\text{fgm}}}, \quad (29)$$

$$\nu_{\text{fgm}} = \frac{3K_{\text{fgm}} - 2\mu_{\text{fgm}}}{2(\mu_{\text{fgm}} + 3K_{\text{fgm}})}. \quad (30)$$

In the present study, the volume fraction of the metal phase follows a simple power function, i.e.,

$$V_{\text{met}}(X) = \left(\frac{X - X_{\text{min}}}{X_{\text{max}} - X_{\text{min}}} \right)^n, \quad (31)$$

where n is the power exponent, X is the gradation direction, and the material properties are graded in the interval $[X_{\text{min}}, X_{\text{max}}]$. Figure 4 shows the volume fraction of the metal phase for various values of n .

The following numerical analysis of crack growth utilizes the properties of a TiB/Ti FGM system. Table 1 lists the relevant material properties of TiB (titanium monoboride) and Ti (commercially pure titanium). The company CERCOM Inc. developed this ceramic/metal FGM system in a layered structural form for armor applications ([24]).

4.2 Cohesive Material Properties. The functionally graded cohesive constitutive model (7) or (18) (three-dimensional case) has the following six independent parameters that characterize the fracture process in a ceramic/metal FGM:

- Γ_{met}^c : local work of separation of metal
- Γ_{cer}^c : local work of separation of ceramic
- σ_{met}^c : peak cohesive traction of metal
- σ_{cer}^c : peak cohesive traction of ceramic

Table 1 Material Properties of Ti and TiB

Materials	Young's modulus (GPa)	Poisson's ratio	J_c (KJ/m ²)	σ_{met}^c (MPa)	δ_{met}^c (mm)	σ_{cer}^c (MPa)	δ_{cer}^c (mm)
Ti	107	0.34	150	620	0.089		
TiB	375	0.14	0.11			4.0	0.01

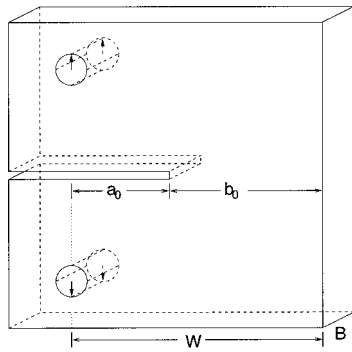


Fig. 5 C(T) specimen geometry

β_{met} and β_{cer} : cohesive gradation parameters.

The calibrated values of Γ_{met}^c and σ_{met}^c are the Griffith energy release rate (under small-scale yielding conditions) and the peak cohesive stress of the metal phase, which generally lies between two to three times the uniaxial yield stress. The first equation of (22) yields the characteristic opening displacement δ_{met}^c . We note that ductile deformations are present in the background material when the cohesive characteristic parameters of the metal are calibrated following the above procedure, however, such deformations are not considered in the present study. Nevertheless, this calibration procedure is used with emphasis on the presentation of the cohesive model and the effects of gradation parameter β_{met} and metal volume fraction V_{met} on the load versus crack growth responses. For the ceramic phase, it is natural to assign the energy release rate to Γ_{cer}^c . For this phenomenological model applicable at engineering scales, the characteristic opening displacement δ_{cer}^c is assumed to be approximately the average grain size of ceramic particles in the ceramic/metal FGM. The peak cohesive traction σ_{cer}^c is therefore determined from the second equation of (22). At smaller length scales, the local nature of the failure mechanism contributes to the characteristic parameters of the cohesive zone model, which may lead to different material parameters and different simulation results of crack growth. Calibration of the other two parameters β_{met} and β_{cer} follows by matching the predicted, with measured, fracture behavior. Table 1 lists the relevant cohesive properties for the TiB/Ti FGM, where the critical J values (J_c , as the cohesive energy) for TiB and Ti are taken from references [25,26].

5 Crack Growth in TiB/Ti Functionally Graded Materials

5.1 Finite Element Models. We performed numerical analyses of crack growth for both C(T) and SE(B) specimens, as illustrated in Figs. 5–6 and Figs. 7–8, respectively. Table 2 summarizes the geometric parameters of the C(T) specimen. The absolute size for the specimen is $W=50$ mm. The initial nondimensional crack length is $a_0/W=0.4$, the initial nondimensional

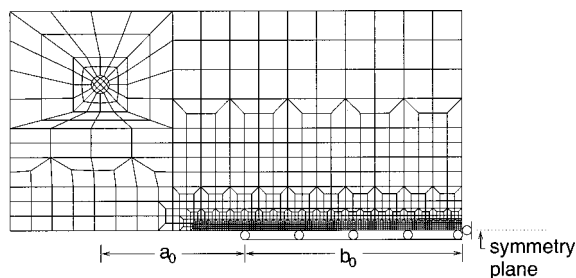


Fig. 6 Typical mesh for analyses of C(T) specimen

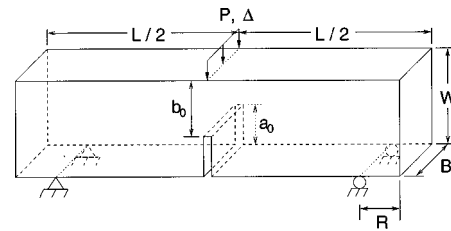


Fig. 7 SE(B) specimen geometry

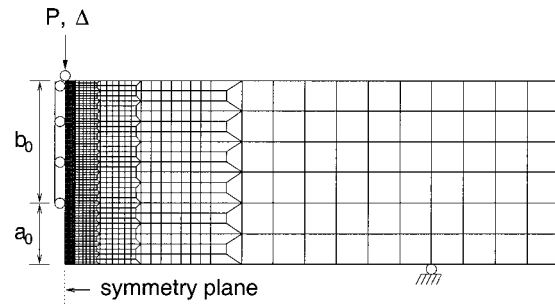


Fig. 8 Typical mesh for analyses of SE(B) specimen

ligament size is then $b_0/W=0.6$, and the thickness is 4.5 mm. Table 3 provides the geometric parameters for the SE(B) specimens. A layered functionally graded material (FGM) version of the SE(B) specimen has been recently tested in [25]. From a modeling point of view, the functionally graded material (FGM) composition varies from 100 percent TiB at the cracked surface to 100 percent Ti at the uncracked surface. Thus the volume fraction of Ti varies from zero at the cracked surface to one at the uncracked surface.

The finite element models consist of eight-node isoparametric solid elements and the eight-node interface-cohesive elements. Due to symmetry considerations, we model only one-quarter of each specimen. Interface-cohesive elements are placed only over the initial uncracked ligament and have a uniform size of 0.25 mm for the C(T) specimen, and 0.1 mm for the SE(B) specimens. The finite element model has eight uniform layers of elements over the half thickness for the C(T) specimen. For the thicker SE(B) specimens, the model has ten uniform layers over the half thickness. Figure 6 shows the front view of the typical finite element mesh for the C(T) specimen and Fig. 8 shows the front view of the finite element mesh for the SE(B) specimens.

5.2 Finite Element Analysis. The FGM modeling features described in this work have been implemented in the fracture mechanics research code WARP3D ([27]). In addition to the conventional solid and interface-cohesive elements for homogeneous materials, this code also incorporates the solid element with

Table 2 Geometric parameters of C(T) specimen

Specimen	W (mm)	B (mm)	a_0/W
C(T)	50	4.5	0.4

Table 3 Geometric parameters of SE(B) specimens

Specimen	L (mm)	W (mm)	B (mm)	a_0/W	R (mm)
SE(B)	79.4	14.7	7.4	0.1, 0.3	10.2

graded elastic properties and the interface-cohesive element coupled with the functionally graded cohesive constitutive model described in Sections 2 and 3.

WARP3D supports the conventional interface-cohesive element for crack growth with adaptive load control, element extinction and other features. Such computational procedures (previously used for homogeneous materials) also prove essential in analyses of FGMs to track accurately the cohesive constitutive response. For the cohesive fracture model proposed in Section 2, the adaptive load control parameter becomes the characteristic opening displacement δ_{met}^c of the metal. The analysis uses a limit of $\Delta\delta/\delta_{met}^c = 0.2$ per load step for adaptive load control, where $\Delta\delta$ is the largest change of effective opening displacement δ experienced by interface-cohesive elements in a given load step. The element extinction occurs when the average opening displacement δ of the element reaches $5\delta_{met}^c$, which corresponds to a cohesive traction less than 10 percent of the peak value of the metal multiplied by the metal volume fraction. Selection of δ_{met}^c (of the metal phase) as the controlling parameter for adaptive load control and element extinction follows from the analyses demonstrating that the metal phase largely controls fracture behavior of the FGM. The cohesive fracture energy of TiB, for example, is less than 0.1 percent of that for Ti.

5.3 Crack Growth in C(T) Specimen. The specimen is loaded by opening displacements applied uniformly through the thickness at the loading pin. Crack growth is taken to occur when the interface-cohesive elements ahead of the crack front satisfy the element extinction condition. Figure 9(a) shows the load versus crack extension curves for the C(T) specimen for various values of β_{met} . The power exponent $n=0.5$ (shape index of the metal volume fraction) defines an overall metal rich specimen. Because the cohesive traction of the ceramic phase is extremely small compared with that of the metal phase for the TiB/Ti FGM studied, the parameter β_{cer} plays a negligible role in determining the cohesive traction of the FGM. Consequently, we take $\beta_{cer} = 1.0$ in the current and all subsequent calculations. Figure 9(a) shows that for a given β_{met} , the load decreases steadily with crack extension in the present analyses which do not include plasticity in the background material. This contrasts with ductile fracture of metals which show load increases with crack extension during initial growth followed by load reductions when strain hardening no longer accommodates the decreasing ligament (see [8] for examples). The figure also shows that for a given crack extension, a larger β_{met} lowers the load. This is consistent with the cohesive fracture model (7) where a larger β_{met} reduces the peak cohesive traction. Figure 9(b) and 9(c) show similar results for the same specimen for $n=1.0$ (a specimen with equal overall metal and ceramic volume fractions) and $n=2.0$ (an overall metal lean specimen), respectively. Comparing the results in the three figures, we observe that the load becomes lower for larger n . The result is expected since a larger n corresponds to a lower metal volume fraction, which results in a lower cohesive energy for the FGM.

Figure 10 shows the load versus crack extension curves for the same C(T) specimen studied in Fig. 9(a) with addition of the crack growth responses for homogeneous metal (Ti) and ceramic (TiB) specimens. These two additional configurations provide bounding solutions for the FGM responses. The load for pure Ti remains larger than those for the TiB/Ti FGM with various β_{met} . The loads during crack extension for the pure TiB, however, remain vanishingly small compared to the FGM.

5.4 Crack Growth in SE(B) Specimen. As a final numerical example, we consider an SE(B) specimen loaded by opening displacements applied uniformly through the thickness at the specimen center plane. A layered FGM version of the specimen has been recently tested ([25]). The first layer of the tested specimen consists of 15 percent Ti and 85 percent TiB, while the last layer (seventh layer) consists of 100 percent Ti. Crack initiation

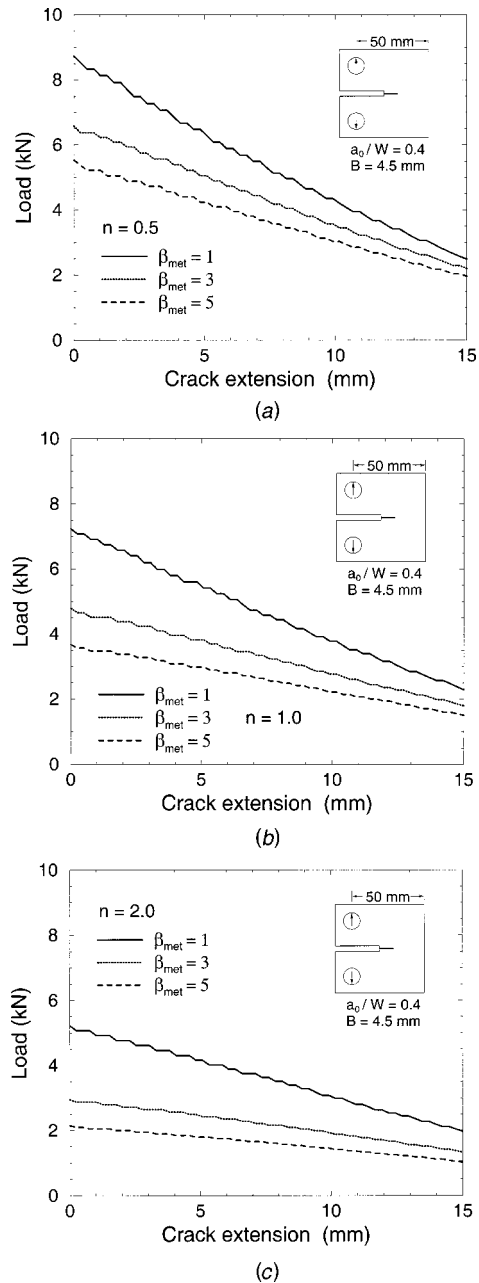


Fig. 9 Load-crack extension response for the C(T) Ti/TiB specimen with $a_0/W=0.4$, $B=4.5$ mm; (a) $n=0.5$; (b) $n=1.0$; (c) $n=2.0$

occurred at a measured load of 920 Newtons (N). The experimental results show that load increases with crack extension during the initial growth and then decreases with further crack extension. The measured load corresponding to a crack growth of 5 mm is about 1200 N. Figure 11 shows the volume fraction of Ti in this TiB/Ti specimen. The dotted (stepped) line shows the property gradation in the experimentally tested specimen. A least-squares approximation yields the power exponent $n=0.84$ in the metal volume fraction function of Eq. (31). Figure 12 shows the numerical results of the load versus crack extension responses for the SE(B) specimen with $\beta_{met}=16$ and $n=0.84$. For the β_{met} selected, the crack initiation load agrees quite closely with the experimentally measured value. Compared with the experimental observations after the crack initiation ([25]), the discrepancy in the trend of load versus crack extension response arises because the present analysis does not consider plasticity in the background

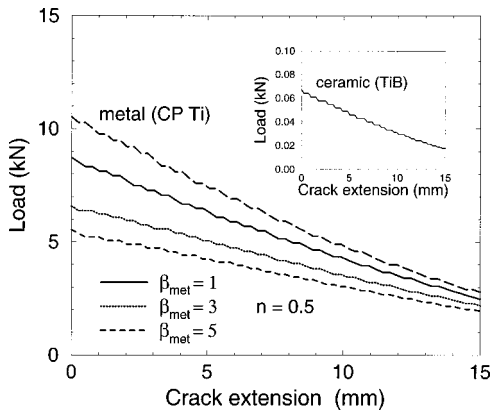


Fig. 10 Load-crack extension response for the C(T) Ti/TiB specimen with $a_0/W=0.4$, $B=4.5$ mm

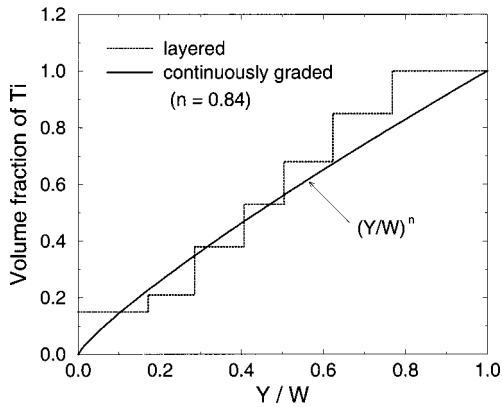


Fig. 11 Volume fraction of Ti in the TiB/Ti functional graded material (FGM)

material. When the plasticity effect is taken into account (work underway by the authors), we expect that the trend of the load versus crack extension will be more consistent with the experimental observations (the calibrated value of β_{met} may be larger than 16). Figure 12 also shows the numerical results of the load versus crack extension for plane-strain and plane-stress models. Though we have not found differences between the two-dimensional and three-dimensional responses, we expect that sig-

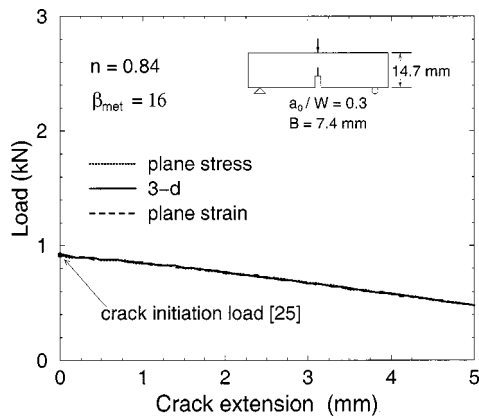


Fig. 12 Load-crack extension response for the SE(B) Ti/TiB specimen with $a_0/W=0.3$, $B=7.4$ mm, $n=0.84$

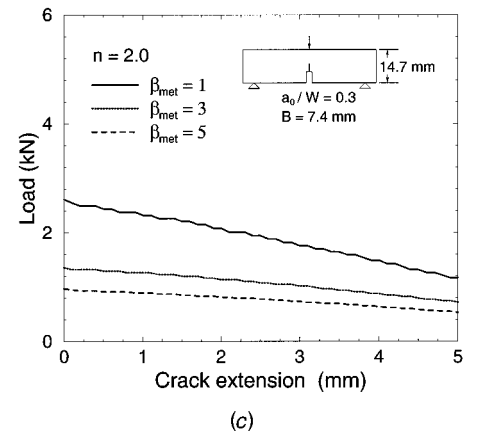
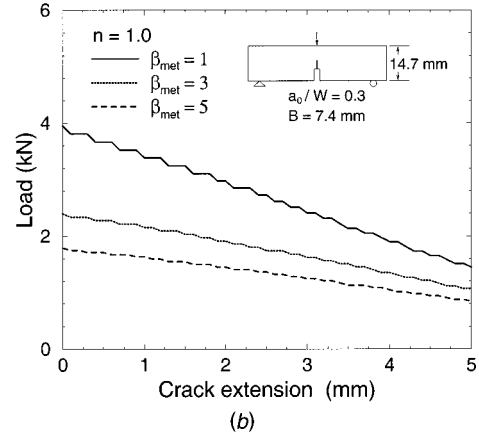
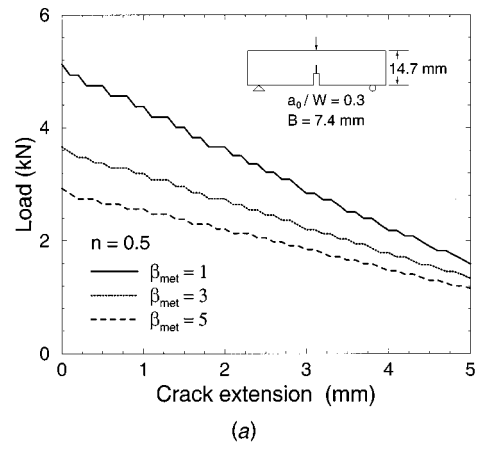


Fig. 13 Load-crack extension response for the SE(B) Ti/TiB specimen with $a_0/W=0.3$, $B=7.4$ mm; (a) $n=0.5$; (b) $n=1.0$; (c) $n=2.0$

nificant differences will develop with plasticity in the background material due to variations in crack front constraint and crack front tunneling.

Figure 13 shows the effect of β_{met} and n on the load versus crack extension responses for the SE(B) specimen. The power exponent n (shape index of the metal volume fraction) is 0.5 in Fig. 13(a), 1.0 in Fig. 13(b), and 2.0 in Fig. 13(c). Similar load versus crack extension behavior to that for the C(T) specimen is observed for the SE(B) specimen, i.e., for a given β_{met} , the load decreases steadily with crack extension; for a given crack extension, a larger β_{met} reduces the load; and finally, the load becomes lower for larger n . Because β_{met} has a pronounced effect on the load versus crack extension responses, we may expect to calibrate the values of β_{met} from experimental observations (see Section 2).

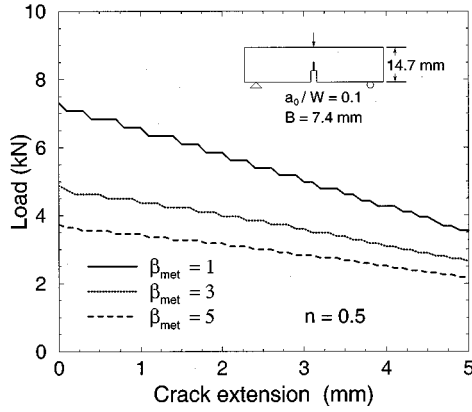


Fig. 14 Load-crack extension response for the SE(B) Ti/TiB specimen with $a_0/W=0.1$, $B=7.4$ mm; and $n=0.5$

Figure 14 shows the load versus crack extension curves for the SE(B) specimen with an initial nondimensional crack length $a_0/W=0.1$. Similar results to that shown in Fig. 13(a) can be observed. Therefore, without considering plasticity in the background material, the load decreases with crack extension due to the decreasing ligament for the laboratory crack size.

6 Concluding Remarks

This study presents a novel phenomenological cohesive fracture model for ceramic/metal functionally graded materials (FGMs) and the corresponding implementation in a three-dimensional finite element method framework. The model has six independent material parameters, i.e., the cohesive energy densities ($\Gamma_{\text{met}}^c, \Gamma_{\text{cer}}^c$), the peak cohesive tractions of the metal and ceramic phases ($\sigma_{\text{met}}^c, \sigma_{\text{cer}}^c$) and two cohesive gradation parameters ($\beta_{\text{met}}, \beta_{\text{cer}}$) to represent approximately the transition between the fracture mechanisms of metal and ceramic phases, respectively. In contrast to existing models that consider only tensile mode fracture, the present model accommodates three-dimensional tensile and shear fracture modes although the numerical examples illustrate only mode I fracture behavior. Applications of the cohesive fracture model to the analysis of crack growth in both C(T) and SE(B) specimens of TiB/Ti FGM show that the load to cause crack extension in the FGM compares to that for a pure metal (Ti) specimen. In the present study, the load decreases steadily with subsequent crack extension, which contrasts with ductile fracture behavior of metals (the present analyses do not admit plasticity in the background material). The results obtained indicate that the cohesive gradation parameter for the metal has a pronounced effect on the load versus crack extension response. This suggests that the parameter may be reasonably calibrated by matching the predicted crack growth response with experimental observations. An extension of this work includes consideration of plasticity in the bulk FGM (background). In this case, we expect to detect strong three-dimensional effects of crack front tunneling and variations in crack front constraint. This investigation is currently being pursued by the authors.

Acknowledgments

This work was sponsored by a grant from the NASA Ames Research Center (NAG 2-1424) to the University of Illinois at Urbana-Champaign. Dr. Tina Panontin serves as the project Technical Monitor. We also acknowledge partial support of NSF under grant No. CMS-0115954 (Mechanics and Materials Program).

Appendix

In finite element analyses, the tangent modulus matrix $D_{ij}(i, j = 1, 2, 3)$ for the cohesive models (18) defined below is needed

$$\dot{\sigma}_i = D_{ij} \dot{v}_j, \quad (32)$$

where $(\sigma_1, \sigma_2, \sigma_3) = (\sigma_{s1}, \sigma_{s2}, \sigma_n)$, $(v_1, v_2, v_3) = (v_{s1}, v_{s2}, v_n)$, and $D_{ij} = \partial \sigma_i / \partial v_j$. Here D_{ij} are the components of \mathbf{D}_{coh} matrix in Eq. (25). The detailed expression for D_{ij} is given as follows. First note that

$$D_{ij} = \frac{\partial}{\partial v_j} \left(\frac{\partial \phi_{\text{fgm}}}{\partial \delta_{\text{eff}}} \frac{\partial \delta_{\text{eff}}}{\partial v_i} \right) = \sigma_{\text{eff}}^2 \frac{\partial^2 \delta_{\text{eff}}}{\partial v_i \partial v_j} + \frac{\partial \sigma_{\text{eff}}}{\partial \delta_{\text{eff}}} \frac{\partial \delta_{\text{eff}}}{\partial v_i} \frac{\partial \delta_{\text{eff}}}{\partial v_j}. \quad (33)$$

It is clear from the above equation that $D_{ij} = D_{ji}$. Use of Eqs (12), (14), and (33) yields

$$\begin{aligned} D_{11} &= \eta^2 \frac{\sigma_{\text{eff}}}{\delta_{\text{eff}}} + \frac{\eta^4 v_1^2}{\delta_{\text{eff}}^2} \left(\frac{\partial \sigma_{\text{eff}}}{\partial \delta_{\text{eff}}} - \frac{\sigma_{\text{eff}}}{\delta_{\text{eff}}} \right), \\ D_{22} &= \eta^2 \frac{\sigma_{\text{eff}}}{\delta_{\text{eff}}} + \frac{\eta^4 v_2^2}{\delta_{\text{eff}}^2} \left(\frac{\partial \sigma_{\text{eff}}}{\partial \delta_{\text{eff}}} - \frac{\sigma_{\text{eff}}}{\delta_{\text{eff}}} \right), \\ D_{33} &= \frac{\sigma_{\text{eff}}}{\delta_{\text{eff}}} + \frac{v_3^2}{\delta_{\text{eff}}^2} \left(\frac{\partial \sigma_{\text{eff}}}{\partial \delta_{\text{eff}}} - \frac{\sigma_{\text{eff}}}{\delta_{\text{eff}}} \right), \\ D_{12} = D_{21} &= \eta^4 \frac{v_1 v_2}{\delta_{\text{eff}}^2} \left(\frac{\partial \sigma_{\text{eff}}}{\partial \delta_{\text{eff}}} - \frac{\sigma_{\text{eff}}}{\delta_{\text{eff}}} \right), \\ D_{13} = D_{31} &= \eta^2 \frac{v_1 v_3}{\delta_{\text{eff}}^2} \left(\frac{\partial \sigma_{\text{eff}}}{\partial \delta_{\text{eff}}} - \frac{\sigma_{\text{eff}}}{\delta_{\text{eff}}} \right), \\ D_{23} = D_{32} &= \eta^2 \frac{v_2 v_3}{\delta_{\text{eff}}^2} \left(\frac{\partial \sigma_{\text{eff}}}{\partial \delta_{\text{eff}}} - \frac{\sigma_{\text{eff}}}{\delta_{\text{eff}}} \right), \end{aligned} \quad (34)$$

where σ_{eff} is given by Eq. (18) and $\partial \sigma_{\text{eff}} / \partial \delta_{\text{eff}}$ is

$$\begin{aligned} \frac{\partial \sigma_{\text{eff}}}{\partial \delta_{\text{eff}}} &= \frac{V_{\text{met}}(\mathbf{x})}{V_{\text{met}}(\mathbf{x}) + \beta_{\text{met}}[1 - V_{\text{met}}(\mathbf{x})]} e \left(\frac{\sigma_{\text{met}}^c}{\delta_{\text{cer}}^c} \right) \left(1 - \frac{\delta_{\text{eff}}}{\delta_{\text{met}}^c} \right) \\ &\times \exp \left(- \frac{\delta_{\text{eff}}}{\delta_{\text{met}}^c} \right) + \frac{1 - V_{\text{met}}(\mathbf{x})}{1 - V_{\text{met}}(\mathbf{x}) + \beta_{\text{cer}} V_{\text{met}}(\mathbf{x})} \\ &\times e \left(\frac{\sigma_{\text{cer}}^c}{\delta_{\text{cer}}^c} \right) \left(1 - \frac{\delta_{\text{eff}}}{\delta_{\text{cer}}^c} \right) \exp \left(- \frac{\delta_{\text{eff}}}{\delta_{\text{cer}}^c} \right), \end{aligned} \quad (35)$$

under loading conditions, and

$$\sigma_{\text{eff}} = \left(\frac{\sigma_{\text{eff}}^{\text{max}}}{\delta_{\text{eff}}^{\text{max}}} \right) \delta_{\text{eff}}, \quad (36)$$

$$\frac{\partial \sigma_{\text{eff}}}{\partial \delta_{\text{eff}}} = \frac{\sigma_{\text{eff}}^{\text{max}}}{\delta_{\text{eff}}^{\text{max}}} \quad (37)$$

for the unloading case.

References

- [1] Hirai, T., 1996, "Functionally Gradient Materials," *Materials Science and Technology: Processing of Ceramics, Part 2*, R. J. Brook eds., VCH Verlagsgesellschaft mbH, Weinheim, Germany, **17B**, pp. 292–341.
- [2] Koizumi, M., 1993, "The Concept of FGMs," *Ceramic Transactions: Functionally Graded Materials*, J. B. Holt, M. Koizumi, T. Hirai, and Z. Munir, eds., American Ceramic Society, Westerville, OH, **34**, pp. 3–10.
- [3] Suresh, S., and Mortensen, A., 1998, *Functionally Graded Materials*, The Institute of Materials, IOM Communications, London.
- [4] Dugdale, D. S., 1960, "Yielding of Steel Sheets Containing Slits," *J. Mech. Phys. Solids*, **8**, pp. 100–104.
- [5] Hillerborg, A., Modeer, M., and Petersson, P. E., 1976, "Analysis of Crack Formation and Crack Growth in Concrete by Means of Fracture Mechanics and Finite Elements," *Cement Concrete Res.*, **6**, pp. 773–782.
- [6] Mosalam, K. M., and Paulino, G. H., 1997, "Evolutionary Characteristic Length Method for Smearred Cracking Finite Element Models," *Finite Elem. Anal. Design*, **27**, pp. 99–108.

- [7] Needleman, A., 1987, "A Continuum Model for Void Nucleation by Inclusion Debonding," *ASME J. Appl. Mech.*, **54**, pp. 525–531.
- [8] Roy, Y. A., and Dodds, Jr., R. H., 2001, "Simulation of Ductile Crack Growth in Thin Aluminum Panels Using 3-D Surface Cohesive Elements," *Int. J. Fract.*, **110**, pp. 21–45.
- [9] Finot, M., Shen, Y.-L., Needleman, A., and Suresh, S., 1994, "Micromechanical Modeling of Reinforcement Fracture in Particle-Reinforced Metal-Matrix Composites," *Metall. Trans. A*, **25**, pp. 2403–2420.
- [10] Jin, Z.-H., and Batra, R. C., 1996, "Some Basic Fracture Mechanics Concepts in Functionally Graded Materials," *J. Mech. Phys. Solids*, **44**, pp. 1221–1235.
- [11] Cai, H., and Bao, G., 1998, "Crack Bridging in Functionally Graded Coatings," *Int. J. Solids Struct.*, **35**, pp. 701–717.
- [12] Williamson, R. L., Rabin, B. H., and Drake, J. T., 1993, "Finite Element Analysis of Thermal Residual Stresses at Graded Ceramic-Metal Interfaces, Part I: Model Description and Geometrical Effects," *J. Appl. Phys.*, **74**, pp. 1310–1320.
- [13] Giannakopoulos, A. E., Suresh, S., Finot, M., and Olsson, M., 1995, "Elasto-plastic Analysis of Thermal Cycling: Layered Materials With Compositional Gradients," *Acta Metall. Mater.*, **43**, pp. 1335–1354.
- [14] Rose, J. H., Ferrante, J., and Smith, J. R., 1981, "Universal Binding Energy Curves for Metals and Bimetallic Interfaces," *Phys. Rev. Lett.*, **47**, pp. 675–678.
- [15] Siegmund, T., and Needleman, A., 1997, "A Numerical Study of Dynamic Crack Growth in Elastic-Viscoplastic Solids," *Int. J. Solids Struct.*, **34**, pp. 769–788.
- [16] Ortiz, M., and Pandolfi, A., 1999, "Finite-Deformation Irreversible Cohesive Elements for Three-Dimensional Crack-Propagation Analysis," *Int. J. Numer. Methods Eng.*, **44**, pp. 1267–1282.
- [17] Tvergaard, V., and Hutchinson, J. W., 1992, "The Relation Between Crack Growth Resistance and Fracture Process Parameters in Elastic-Plastic Solids," *J. Mech. Phys. Solids*, **40**, pp. 1377–1392.
- [18] Guinea, G. V., Elices, M., and Planas, J., 1997, "On the Initial Shape of the Softening Function of Cohesive Materials," *Int. J. Fract.*, **87**, pp. 139–149.
- [19] Camacho, G. T., and Ortiz, M., 1996, "Computational Modelling of Impact Damage in Brittle Materials," *Int. J. Solids Struct.*, **33**, pp. 2899–2938.
- [20] Kim, J.-H., and Paulino, G. H., 2002, "Finite Element Evaluation of Mixed Mode Stress Intensity Factors in Functionally Graded Materials," *Int. J. Numer. Methods Eng.*, **53**, pp. 1903–1935.
- [21] Cook, R. D., Malkus, D. S., and Plesha, M. E., 1989, *Concepts and Applications of Finite Element Analysis*, 3rd Ed., John Wiley and Sons, New York.
- [22] Reiter, T., Dvorak, G. J., and Tvergaard, V., 1997, "Micromechanical Models for Graded Composite Materials," *J. Mech. Phys. Solids*, **45**, pp. 1281–1302.
- [23] Hill, R., 1965, "A Self-Consistent Mechanics of Composite Materials," *J. Mech. Phys. Solids*, **13**, pp. 213–222.
- [24] Nelson, G., and Ezis, A., 1996, "Functionally Graded Material (FGM) Armor in the TiB/Ti system (U)," *CERCOR Report*, Vista, CA.
- [25] Carpenter, R. D., Liang, W. W., Paulino, G. H., Gibeling, J. C., and Munir, Z. A., 1999, "Fracture Testing and Analysis of a Layered Functionally Graded Ti/TiB Beam in 3-Point Bending," *Mater. Sci. Forum*, **308–311**, pp. 837–842.
- [26] Liang, W. W., 1999, "Finite Element Analysis of Model I Crack Propagation in Layered Functionally Graded Materials," M.Sc. thesis, University of California, Davis, CA.
- [27] Gullerud, A. S., Koppenhoefer, K. C., Roy, A., and Dodds, Jr., R. H., 2000, *WARP3D—Release 13.8 Manual*, Civil Engineering, Report No. UILU-ENG-95-2012, University of Illinois, Urbana, IL.